

MIT Open Access Articles

Inhibited proton transfer enhances Au-catalyzed CO₂-to-fuels selectivity

The MIT Faculty has made this article openly available. **Please share** how this access benefits you. Your story matters.

Citation: Wuttig, Anna et al. "Inhibited Proton Transfer Enhances Au-Catalyzed CO₂-to-Fuels Selectivity." Proceedings of the National Academy of Sciences 113.32 (2016): E4585–E4593. © 2016 National Academy of Sciences

As Published: <http://dx.doi.org/10.1073/pnas.1602984113>

Publisher: National Academy of Sciences (U.S.)

Persistent URL: <http://hdl.handle.net/1721.1/107143>

Version: Final published version: final published article, as it appeared in a journal, conference proceedings, or other formally published context

Terms of Use: Article is made available in accordance with the publisher's policy and may be subject to US copyright law. Please refer to the publisher's site for terms of use.



Inhibited proton transfer enhances Au-catalyzed CO₂-to-fuels selectivity

Anna Wuttig^a, Momo Yaguchi^{b,c}, Kenta Motobayashi^{b,1}, Masatoshi Osawa^b, and Yogesh Surendranath^{a,2}

^aDepartment of Chemistry, Massachusetts Institute of Technology, Cambridge, MA 02139; ^bInstitute for Catalysis, Hokkaido University, Sapporo 001-0021, Japan; and ^cGraduate School of Environmental Science, Hokkaido University, Sapporo 060-0810, Japan

Edited by Daniel G. Nocera, Harvard University, Cambridge, MA, and approved June 7, 2016 (received for review February 22, 2016)

CO₂ reduction in aqueous electrolytes suffers efficiency losses because of the simultaneous reduction of water to H₂. We combine in situ surface-enhanced IR absorption spectroscopy (SEIRAS) and electrochemical kinetic studies to probe the mechanistic basis for kinetic bifurcation between H₂ and CO production on polycrystalline Au electrodes. Under the conditions of CO₂ reduction catalysis, electrogenerated CO species are irreversibly bound to Au in a bridging mode at a surface coverage of ~0.2 and act as kinetically inert spectators. Electrokinetic data are consistent with a mechanism of CO production involving rate-limiting, single-electron transfer to CO₂ with concomitant adsorption to surface active sites followed by rapid one-electron, two-proton transfer and CO liberation from the surface. In contrast, the data suggest an H₂ evolution mechanism involving rate-limiting, single-electron transfer coupled with proton transfer from bicarbonate, hydronium, and/or carbonic acid to form adsorbed H species followed by rapid one-electron, one-proton, or H recombination reactions. The disparate proton coupling requirements for CO and H₂ production establish a mechanistic basis for reaction selectivity in electrocatalytic fuel formation, and the high population of spectator CO species highlights the complex heterogeneity of electrode surfaces under conditions of fuel-forming electrocatalysis.

carbon dioxide reduction | catalyst selectivity | in situ spectroscopy | proton-coupled electron transfer

Product selectivity is a principal design consideration for the development of practical catalysts. Catalyst selectivity is dictated by (i) the relative free energy barriers for progress along competing reaction pathways and (ii) the relative rates of reactant delivery to active sites (1). Enzymes fine tune these parameters with exquisite precision to achieve selectivity (2). Nature augments the coordination environment of metallocofactor active sites to optimize the binding strengths of reaction partners and preorganizes reaction participants toward low-barrier pathways (3). Additionally, many active sites reside at the terminus of molecular channels that gate the coordinated delivery of substrates (4, 5) required for selective transformations. Efforts to prepare artificial catalysts with product selectivities rivaling that of nature require a detailed understanding of these factors.

Currently, our understanding of how to systematically modulate selectivity in heterogeneous catalysts remains poor (6–8). Unlike (bio)molecular catalysts, which ideally consist of a uniform ensemble of active sites, heterogeneous catalysts consist of a nonuniform distribution of surface sites (9), requiring an understanding of which are active and which are dormant. The surface site distribution is strongly dependent on the surface nanostructure, oxidation state, and degree of restructuring (7). Superimposed on this distribution are the rate-limiting elementary reaction steps that dictate kinetic branching ratios at surface active sites (10). For catalysis mediated by electrode surfaces, these factors are subject to change as a function of the applied potential (11, 12), and the log-linear relationship between reaction rate and potential often introduces severe transport limitations that further augment the intrinsic reaction kinetics (13). Disentangling these correlated processes is essential to the development of selective electrocatalysts.

Electrocatalytic CO₂ reduction (CDR) allows for the storage of intermittent renewable electricity in energy-dense carbonaceous fuels (14–17). CDR is most practically conducted in aqueous electrolytes, in which the undesirable reduction of protons to H₂ presents a principal selectivity challenge. Because the hydrogen evolution reaction (HER) is thermodynamically accessible over the same potential range as nearly all CDR reaction products (18–20), selective fuel formation relies on the electrode's ability to control the relative rates of these competing pathways.

Computational investigations of CDR selectivity have largely applied the Sabatier principle, which states that an optimal catalyst is one that binds key intermediates neither too strongly nor too weakly (21). Within this framework, the relative binding energies of adsorbed H and CO, proposed intermediates along HER and CDR pathways, respectively (22–30), serve as descriptors for the relative rates of each reaction. Computational studies have highlighted that H and CO display differing affinities for surface features, including terraces, edges, and corners (22, 23, 29–31), suggesting a wide distribution of adsorbate binding energies on the polycrystalline metal surfaces that have been the subject of most CDR investigations (18, 32). Additionally, coadsorption of electrolyte ions and CO can play a dominant role in both CO (25, 29, 30, 33, 34) and H adsorption (24, 26, 29). Despite the contemporary emphasis on adsorbate binding energies as key determinants of selectivity in fuel synthesis, the surface adsorbate population has yet to be probed spectroscopically in situ under the conditions of CDR catalysis.

In electrocatalytic reactions, substrate bond activation is accompanied by electron transfer (ET) from the electrode. The

Significance

Renewable electricity can be stored in the energy-dense bonds of carbon-based fuels via the electroreduction of CO₂. CO₂ reduction in aqueous electrolytes suffers efficiency losses because of the simultaneous reduction of water to H₂. Rational design of selective CO₂-to-fuels catalysts requires direct knowledge of the electrode surface structure during turnover and how electrons and protons couple to direct product selectivity. Using model Au catalysts, we uncover the complex heterogeneity in CO surface binding equilibria and the differential proton coupling requirements for CO vs. H₂ production. We assemble the spectroscopic and kinetic data to construct a mechanistic model that predicts that impeding proton transfer to the surface is an effective strategy for improving CO₂-to-fuels catalyst selectivity.

Author contributions: A.W. and Y.S. designed research; A.W. and M.Y. performed research; K.M. and M.O. contributed new reagents/analytic tools; A.W., M.Y., M.O., and Y.S. analyzed data; and A.W., M.Y., M.O., and Y.S. wrote the paper.

The authors declare no conflict of interest.

This article is a PNAS Direct Submission.

¹Present address: Department of Engineering Physics, Electronics, and Mechanics, Nagoya Institute of Technology, Nagoya 466-8555, Japan.

²To whom correspondence should be addressed. Email: yogi@mit.edu.

This article contains supporting information online at www.pnas.org/lookup/suppl/doi:10.1073/pnas.1602984113/-DCSupplemental.

barrier to this ET is augmented by the applied overpotential. Thus, the relative driving force/rate scaling factors (the transfer coefficients) for HER vs. CDR will impact selectivity, even in the limit of identical adsorption energies for key intermediates and a common active site for both reactions. However, the transfer coefficients for HER and CDR occurring concurrently have yet to be probed unambiguously because both reactions are subject to significant transport limitations that mask the activation-controlled kinetics. In particular, because the CDR and HER both consume protons, the pH local to the surface becomes more alkaline than that of the bulk (18, 35, 36). As a result, the buffer strength of the electrolyte strongly impacts the CDR product distribution (37–40). In addition, we have shown that H₂ production can be selectively suppressed relative to CO production by increasing the thickness of ordered porous gold (Au) electrodes (41). Although these studies suggest the importance of transport limitations in determining CDR catalytic selectivity, the mechanistic basis for kinetic branching remains poorly understood.

Herein, we examine the mechanistic basis for CDR vs. HER selectivity on polycrystalline Au surfaces. Because Au surfaces principally generate CO and H₂ (42, 43), they provide an ideal platform for probing reaction selectivity. To probe this bifurcation, we combine for the first time, to our knowledge, in situ surface-enhanced IR absorption spectroscopy (SEIRAS) in an attenuated total reflection (ATR) configuration (44–48) with electrokinetic studies that account for transport effects to formulate a mechanistic model that describes the surface adsorbate population and rate-limiting processes for both reactions. Under conditions relevant to CDR catalysis, we observe that CO is irreversibly bound to a significant fraction of the surface, whereas (bi)carbonate desorbs from the surface. Against this backdrop, we find that CDR is gated by rate-limiting single ET to CO₂ and that the ET is not coupled to proton transfer (PT) from hydronium, bicarbonate, or carbonic acid. However, these species are competent proton donors for forming adsorbed H in the rate-limiting step of HER, establishing that the divergent proton coupling requirements for these two reactions underpin reaction selectivity.

Results and Discussion

Surface Adsorbate Population and Dynamics During CDR. In situ surface-enhanced IR absorption (SEIRA) spectra of Au films provide insight into the surface adsorbates prevalent during CDR catalysis. A SEIRAS-active polycrystalline Au film was prepared on a silicon (Si) prism (experimental details are in *SI Materials and Methods*) and exhibited a roughness factor of ~ 5 as determined by copper (Cu) underpotential deposition (UPD) (Fig. S1, red), consistent with previous literature reports (49). The rough metallic electrode surface amplifies IR absorption by adsorbed molecules. In line with the surface selection rule, the transition dipole moments of adsorbate vibrational modes that are observed must have components perpendicular to the electrode surface (44–48). Although SEIRAS bears close resemblance to surface-enhanced Raman scattering, the latter is known to give rise to inhomogeneous amplification of Raman scattering at hot spots on surface features of high local curvature (50, 51), making it hard to discern whether spectral observables accurately reflect the adsorbate population across the entire surface. In contrast, experimental data on CO adsorption to platinum (Pt) surfaces suggest that SEIRA spectra reflect the aggregate adsorbate speciation (52), do not perturb band positions relative to those observed in IR absorption spectroscopy measurements (53), and give rise to spectral intensities that scale linearly with adsorbate coverage (54, 55). Given this literature precedent, we take our SEIRA spectra as representative of the aggregate adsorbate population and speciation on the entire electrode surface.

SEIRA spectra reveal the potential-dependent adsorption dynamics of the principal electrolyte species (bi)carbonate and water. In CO₂-saturated 0.1 M NaHCO₃ electrolyte, CDR catalysis

onsets at -0.80 V [all potentials are reported vs. the standard hydrogen electrode (SHE)] on polycrystalline Au electrodes (indicated by yellow shading in Fig. 1) (43, 56). The background spectrum was recorded at 0.80 V in CO₂-saturated 0.1 M NaHCO₃ (Fig. 1A), and after polarizing to 0.60 V, a positive band at $1,456$ cm⁻¹ is observed, attributed to adsorbed bicarbonate. Scanning the potential to negative values gives rise to a bleach at $1,460$ cm⁻¹ and a rising band at $1,614$ cm⁻¹ in the corresponding SEIRA spectrum (Fig. 1B). Both the rise and bleach are reversed upon scanning back to positive potentials, indicating that these processes are reversible. Based on literature precedent (57, 58), we assign the peak at $1,460$ cm⁻¹ to (bi)carbonate that is adsorbed to the Au surface at positive potentials. As expected, when negatively polarized, the electrode repels this negatively charged anion, causing its desorption and the corresponding bleach at the same band position. We assign the peak at $1,614$ cm⁻¹ to the δ HOH bending mode of adsorbed water (59–61), and its intensity is anticorrelated to the surface population of adsorbed bicarbonate, suggesting that water adsorption takes the place of adsorbed carbonate under the reducing potentials of CDR catalysis. Interestingly, the δ HOH mode of adsorbed water is red-shifted by 31 cm⁻¹ relative to that of bulk water ($\sim 1,645$ cm⁻¹), attributed to a decrease in hydrogen bonding between water molecules arranged at the surface (59).

In situ SEIRA spectra also reveal that CO is bound to the Au electrode surface during CDR catalysis. At -0.40 V, bands are observed at $2,046$ and $1,977$ cm⁻¹, attributed to electrogenerated CO bound on the Au surface in two distinct environments. In line with literature reports and our own experimental data (Fig. S2), the $2,046$ - and $1,977$ -cm⁻¹ bands display Stark shifts of 50 and 74 cm⁻¹ V⁻¹, respectively, with bands red-shifting with polarization to more negative potentials. Accounting for the Stark shift (62–64), these band positions are in line with experimental vibrational frequency ranges that have been assigned to terminally (CO_{atop}) and bridge-bonded CO (CO_{bridge}) on Au surfaces, respectively (49, 65–68). Although Stark effects prevent a direct comparison of the absolute peak positions observed experimentally under polarization with those computed in the absence of an interfacial field, computed frequency separations of 80 – 152 cm⁻¹ (69–73) between these two binding modes are in line with the 80 - to 90 -cm⁻¹ separation observed here. The stretching frequencies of CO_{bridge} on Au surfaces are higher than the $1,850$ – $1,700$ cm⁻¹ range typical of μ^2 -CO species found in discrete coordination/cluster compounds (74), suggesting that these surface species retain an intermediate bond order between two and three and may exist in a semi-bridging mode. We note that the geometrical preference for CO on Au is highly dependent on the electrolyte conditions (68, 73, 75), and these data provide the first insights, to our knowledge, into CO adsorption at the intermediate pH conditions relevant to CDR catalysis.

Atop adsorption of CO occurs reversibly on Au surfaces under the conditions of CDR catalysis. Under CO₂/CO cosaturation conditions (0.1 M NaHCO₃ electrolyte saturated with 0.5 atm CO and 0.5 atm CO₂), the CO_{atop} band rises and falls over the same potential range (-0.42 to 0.20 V) in the forward and reverse traces (Fig. 1H), indicating reversible CO_{atop} adsorption to Au. Data presented in Fig. S3 additionally support the reversibility of CO_{atop} adsorption. Under CO-free conditions, after the electrode is rapidly switched back to the open circuit potential (0.36 V) after polarization at a potential where CO is evolved (-1.00 V) (Fig. S3A), the integrated CO_{atop} peak intensity declines rapidly over the first three SEIRA spectra (over 1.7 s) (Fig. S3B). This decline is attributed to CO_{atop} desorption from the Au surface as the equilibrium concentration of electrogenerated CO in the vicinity of the electrode diminishes because of diffusion and convection away from the surface. Importantly, this decline in CO_{atop} is not accompanied by a rise in CO_{bridge} population (Fig. S3B), supporting the notion that CO_{atop} desorbs as gaseous CO (CO_g) rather than by its interconversion to CO_{bridge}. This observation, taken

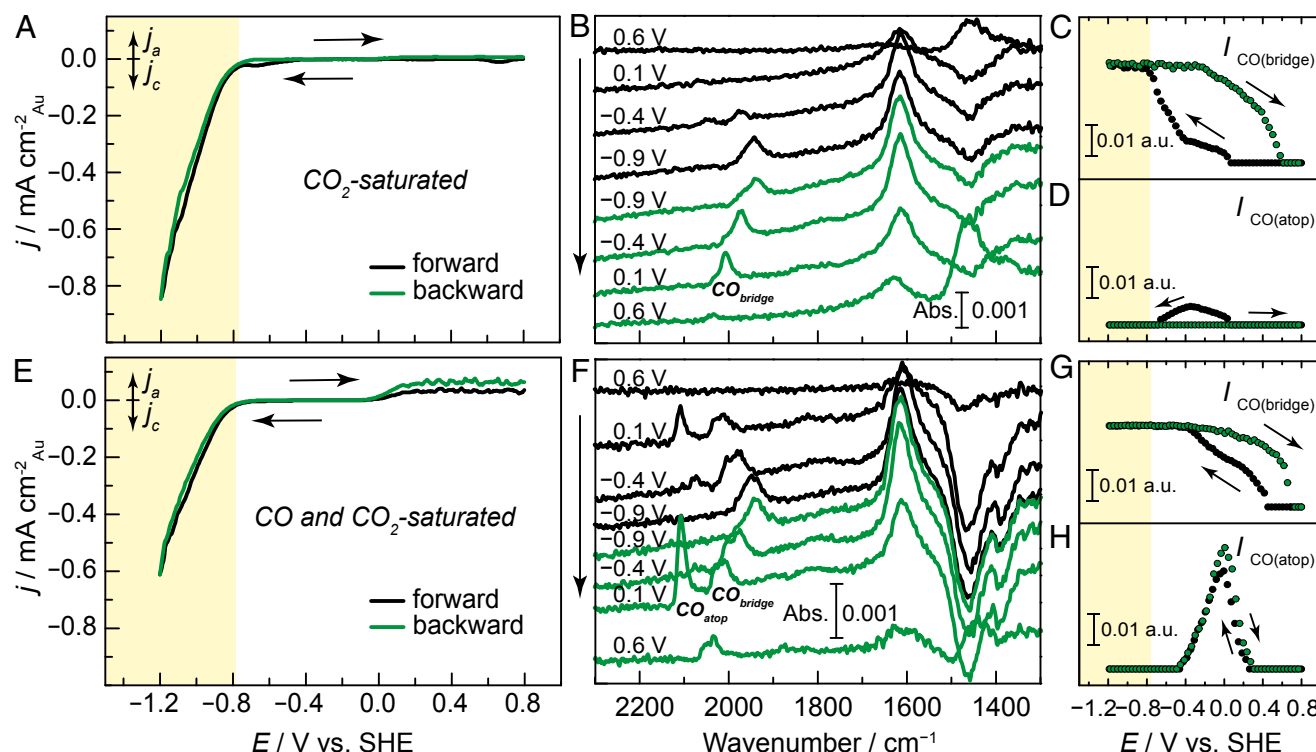


Fig. 1. Potential-dependent adsorption dynamics of principal electrolyte species and CO. Cyclic voltammograms obtained at 10 mV s^{-1} in (A) CO_2 -saturated 0.1 M NaHCO_3 , (B) simultaneously acquired SEIRA spectra, and corresponding integrated band intensities for adsorbed (C) $\text{CO}_{\text{bridge}}$ and (D) CO_{atop} species. Cyclic voltammograms obtained at 10 mV s^{-1} in (E) CO - and CO_2 -saturated 0.1 M NaHCO_3 , (F) simultaneously acquired SEIRA spectra, and corresponding integrated band intensities for adsorbed (G) $\text{CO}_{\text{bridge}}$ and (H) CO_{atop} species. Background spectra were recorded at 0.80 V for both conditions. The potential regime where cathodic catalytic current is observed is highlighted in yellow for clarity.

together with the reversibility of CO_{atop} adsorption between the forward and reverse potential scans (Fig. 1H), suggests that the decline in CO_{atop} peak intensity observed at potentials more negative than 0.00 V is also caused by CO_{atop} desorption as CO_{g} rather than its conversion to $\text{CO}_{\text{bridge}}$. If CO_{atop} and $\text{CO}_{\text{bridge}}$ species were interconverting on the timescale of the measurement, the observed hysteresis in the latter (see below) (Fig. 1G) would give rise to a similar hysteresis in the former, which we do not observe (Fig. 1H). To the best of our knowledge, the observed desorption of CO_{atop} at negative potentials is unprecedented and motivates additional investigation to identify its origin. Nonetheless, the potential regime where CO_{atop} is bound to the surface is positive of the thermodynamic potentials for HER ($E^0 = -0.42 \text{ V}$) and CDR ($E^0 = -0.51 \text{ V}$) under these conditions. Together, our SEIRAS data indicate that CO_{atop} species (i) bind reversibly to the electrode surface and (ii) exist in low surface population at the potentials relevant to CDR catalysis.

In contrast, bridge adsorption of CO occurs irreversibly on Au surfaces under the conditions of CDR catalysis. Fig. 1C and G reveal dramatic hystereses in the $\text{CO}_{\text{bridge}}$ population between negative- and positive-going scans, in line with irreversible adsorption. Data presented in Fig. S3 additionally support this irreversibility. Under CO-free conditions, after the electrode is rapidly switched back to open circuit (0.36 V) after polarization at a potential relevant to CDR catalysis (-1.00 V) (Fig. S3A), the $\text{CO}_{\text{bridge}}$ peak remains present indefinitely (Fig. S3B). Indeed, whether CO is electrogenerated (Fig. 1C) or codosed (Fig. 1G), $\text{CO}_{\text{bridge}}$ remains on the Au surface up until potentials are sufficiently positive to induce its two-electron oxidative desorption as CO_2 (see the following paragraph) (66, 67, 75–78). Notably, the irreversibility of $\text{CO}_{\text{bridge}}$ adsorption promotes its formation 510 mV positive of the thermodynamic E^0 of CDR to CO_{g}

(-0.51 V) under these conditions (Fig. 1C). This 510-mV difference places a lower limit on the CO adsorption energy of these irreversibly bound species. We note that a minority population of CO_{atop} is also electrogenerated at 0.51 V (Fig. 1D), but it is only observed on the initial negative-going scan of the electrode, implying that the surfaces are subject to reconstruction during CDR catalysis. Nonetheless, on polarization to potentials relevant to CDR catalysis, we observe (i) that electrogenerated $\text{CO}_{\text{bridge}}$ is the predominant surface species and (ii) that it is irreversibly bound to the surface.

To estimate the surface coverage of irreversibly adsorbed electrogenerated $\text{CO}_{\text{bridge}}$ species observed in Fig. 1B and C, we performed CO oxidative stripping analysis of a Au rotating cone electrode (RCE). An RCE (79) was used so that CO released from the surface would be swept away by rotation. In Fig. 2, solid line, the first cyclic voltammogram (CV) scan initiated after CDR catalysis on the RCE at -0.80 V displays a broad oxidation wave spanning -0.20 to 0.80 V , in line with reported potentials for two-electron CO oxidation to CO_2 on Au surfaces (66, 67, 75–78). On subsequent cycling (Fig. 2, dotted line), the broad wave is replaced by diminished background waves attributed to (bi)carbonate adsorption to the Au surface. Importantly, the onset potential of CO oxidation, -0.20 V , observed in the CV (Fig. 2) is the same potential at which we observe a decline in $\text{CO}_{\text{bridge}}$ peak intensity in SEIRA spectra (Fig. 1C). In addition, this oxidative CV feature was still observed after a significant time delay ($>1 \text{ min}$) after CDR catalysis, suggesting that $\text{CO}_{\text{bridge}}$, unlike CO_{atop} , is only removed through oxidative conversion to CO_2 rather than desorption as CO_{g} . Together, these data lead us to assign this wave solely to the two-electron oxidation of $\text{CO}_{\text{bridge}}$ species to CO_2 . Using the second scan as a baseline, we quantified the excess charge passed in the initial oxidative feature through relative

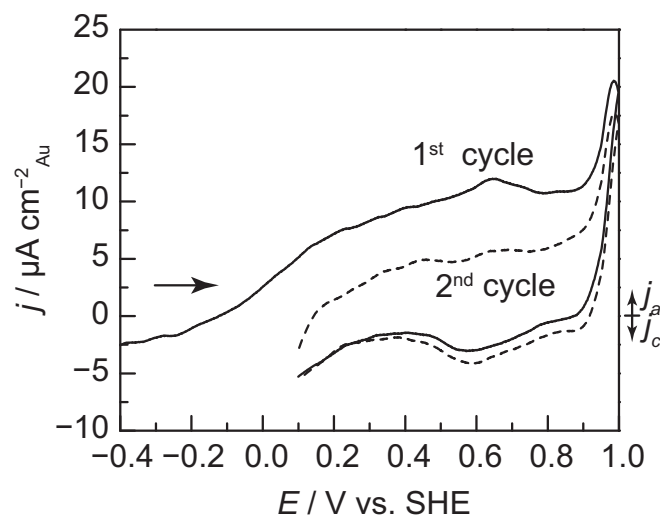


Fig. 2. The first (solid line) and second (dotted line) CV cycles recorded after 7 min of CDR catalysis at -0.80 V in CO_2 -saturated 0.1 M NaHCO_3 at $1,000$ rpm on a Au RCE.

integration of the CV waves (details are in *SI Materials and Methods* and Fig. S4) and estimated a surface concentration, $\Gamma_{\text{CO-bridge}}$, of $0.4 \text{ nmol cm}^{-2}_{\text{Au}}$. Full monolayer adsorption of CO to Au(110) – (1×2) has been shown to give rise to a surface concentration of $\Gamma_{\text{CO,max}} = 1.8 \text{ nmol cm}^{-2}$ (68), suggesting that polycrystalline Au surfaces have a $\text{CO}_{\text{bridge}}$ surface coverage of $\theta_{\text{CObridge}} = \Gamma_{\text{CO-bridge}}/\Gamma_{\text{CO,max}} \sim 0.2$ under CDR catalysis. In Fig. 2, we note the presence of an oxidative feature more positive than 0.90 V vs. SHE that is correlated with the reductive feature spanning 0.50 to 0.90 V vs. SHE. These features are attributed to Au surface oxide formation and back reduction, and they do not affect the behavior of irreversible stripping of adsorbed CO (Fig. S4B).

CO Evolution Rate Is Independent of the Proton Donor Environment.

The relationship between potential and the rate of CO evolution (j_{CO}) was probed over the potential range, -0.80 to -1.00 V, corresponding to overpotentials (η) between 290 and 490 mV for CDR to CO. These data, taken together with studies of the reaction order with respect to bicarbonate concentration ($[\text{HCO}_3^-]$), pH, CO_2 partial pressure (P_{CO_2}), and CO partial pressure (P_{CO}), provide the basis for mechanistic interpretation of CO production catalyzed by polycrystalline Au surfaces. Au electrodes used for kinetic studies exhibited similar surface faceting, Tafel slopes, and j_{CO} relative to SEIRAS-active Au films (Fig. S5), suggesting that the interfacial adsorbate structures described above are also present on the Au electrodes used for the electrokinetic studies described here; j_{CO} values were extracted from the total measured current using in-line GC analyses (full experimental details are in *SI Materials and Methods*) and were normalized to the electrochemically active surface area (Fig. S1, blue) as determined by Cu UPD (80). Fig. S6 shows that j_{CO} remains unaltered when the rotation rate of the Au electrode increases, suggesting that j_{CO} is not inhibited by mass transport under the conditions examined in this study. Thus, we take the data collected in Fig. 3 as direct measurements of activation-controlled rates for CO production.

The current–voltage (Tafel) data combined with the reaction order in P_{CO_2} support a mechanistic sequence involving rate-limiting single ET to CO_2 . The Eyring equation defines an exponential relationship between the activation barrier and reaction rate. Polarizing the electrode to greater η directly reduces the activation barrier for the reaction, leading to an exponential increase in the rate of CO evolution as observed in Fig. 3A. For a mechanistic sequence involving a single rate-limiting ET from

the catalyst resting state, the current is proportional to $\exp(\beta\eta F/RT)$ (81) (i.e., a limiting case of the Butler–Volmer equation at high η , where β is the symmetry factor for the reaction and the other constants take their usual meaning). For outer-sphere interfacial ET reactions, Marcus theory provides a direct estimate for β as a function of driving force and reorganization energy, λ (82). In particular, a β -value equal to 0.5 is expected for outer-sphere ET reactions for which λ is large relative to η . Although a Marcus-type model does not explicitly treat the case of inner-sphere ET reactions at interfaces, β -values of 0.5 have been observed in surface electrocatalysis (13). At modest η , the Tafel data in Fig. 3A display linearity and a slope of 140 mV per decade (dec), corresponding to a β -value of 0.4 , in line with that expected for a rate-limiting single ET. The Tafel slopes observed here are similar to those observed previously for Au-catalyzed CDR (43, 56, 83–85). In addition, j_{CO} is approximately first order in P_{CO_2} across the same potential range of linear Tafel data collection (Fig. 3B), consistent with previous reports in bicarbonate (43) and phosphate (42) electrolytes. These order data taken together with the Tafel slope suggest that CO production proceeds via rate-limiting single ET to CO_2 .

CDR catalysis is zeroth order (Fig. 3C and D) in all other electrolyte constituents over the entire range of linearity of the Tafel data. The rate of CO production is insensitive to the $[\text{HCO}_3^-]$ (Fig. 3C). At constant P_{CO_2} , a change in $\log[\text{HCO}_3^-]$ also alters the pH by 1 unit (18); thus, this experiment alone does not rule out the possibility that the bicarbonate order is positive, whereas the pH order is negative and of the same magnitude, canceling each other out. However, the pH also declines with increasing P_{CO_2} at fixed $[\text{HCO}_3^-]$ (18). Thus, any intrinsic negative order in pH would be reflected in an increase in the CO_2 order to a value greater than one, which we do not observe (Fig. 3B). We, therefore, take the data in Fig. 3C as evidence that j_{CO} is zeroth order in both pH and bicarbonate. These results are consistent with studies in phosphate buffer (42), in which no pH dependence was observed for Au-catalyzed CDR. In addition, the j_{CO} does not depend on the ratio of hydrogen/deuterium (H/D) in the electrolyte (Fig. 3D). We note that changing the H/D ratio can alter the pK_a of the proton donors, but because we observe no dependence on $[\text{HCO}_3^-]$ or pH, neither of these effects convolute the observed absence of an H/D kinetic isotope effect (KIE). Together, the order data in

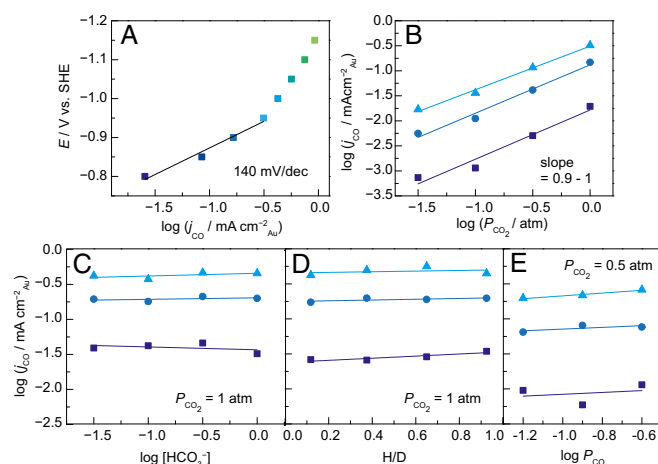


Fig. 3. Electrokinetic data for CO evolution catalysis. (A) CO partial current density–voltage (Tafel) behavior of Au foil in CO_2 -saturated 0.1 M NaHCO_3 electrolyte. (B) P_{CO_2} dependence of the CO partial current density at -0.80 V (dark blue), -0.90 V (teal), and -1.00 V (sky blue) recorded in 0.1 M NaHCO_3 electrolyte. (C) Bicarbonate concentration, (D) $[\text{NaHCO}_3]/[\text{NaHCO}_3]$, and (E) P_{CO} dependences of CO partial current density at -0.80 V (dark blue), -0.90 V (teal), and -1.00 V (sky blue) recorded in CO_2 -saturated bicarbonate electrolyte.

Fig. 3 *C* and *D* suggest that the principal electrolyte constituents are not involved in the mechanistic sequence up to and including the rate-limiting step of catalysis.

CDR catalysis on Au generates CO, which may be expected to inhibit its production, particularly given the high population of adsorbed CO observed by SEIRAS (Fig. 1). To probe whether CO is a component of the rate expression for CDR, we examined j_{CO} as a function of P_{CO} . However, this measurement requires an alternative method for product detection because electro-generated CO is dwarfed by the CO stream and therefore, cannot be quantified directly by in-line GC detection of CO. Because Au electrodes are known to predominantly generate CO and H₂ with >95% cumulative Faradaic efficiency and because the CO and H₂ Faradaic efficiencies add to near unity under our experimental conditions, the H₂ partial current (j_{H_2}) can be subtracted from the total observed current (j_{TOT}) to indirectly measure j_{CO} . The pH of the solution was kept at 7.1 by maintaining the P_{CO_2} at 0.5 atm, whereas the P_{CO} was varied by Ar dilution. We observe that indirectly measured j_{CO} is zeroth order in P_{CO} (Fig. 3*E*), indicating that minor equilibrium CO dissociation from the surface does not precede CO₂ activation under these conditions.

The data in Fig. 3 are consistent with an electrochemical rate law described by the following expression (also shown schematically in Fig. 4*A*):

$$j_{\text{CO}} = k_1 \theta_{\text{CDR}} P_{\text{CO}_2} \exp \frac{\beta EF}{RT}, \quad [1]$$

where k_1 is a potential-independent constant. The rate expression shows the first-order dependence in P_{CO_2} as well as the zeroth-order dependence in pH, $[\text{HCO}_3^-]$, and P_{CO} . This rate law also includes an exponential term that captures the potential-dependent rate of an irreversible single ET step. In Eq. 1, θ_{CDR} is the surface coverage of CDR active sites, which is defined as the ratio of the surface concentration of CDR active sites, Γ_{CDR} , to the total number of Au surface sites, Γ_{Au} . Thus, this value must be between zero and one.

The foregoing rate expression is consistent with a mechanistic model for CDR catalysis that involves rate-limiting ET to CO₂ to form an adsorbed Au-COO⁻ species. This species then undergoes rapid one ET, two PT to liberate water and generate CO, which rapidly dissociates from the surface to regenerate the active site for subsequent turnover (Fig. 4*A*). Importantly, our mechanistic model invokes that reductive adsorption of CO₂ is not concerted with PT as previously postulated (18, 43, 56, 83). The lack of dependence on pH and bicarbonate explicitly excludes a PT/ET

sequence, in which the PT resides in quasiequilibrium, as well as a concerted proton electron transfer (CPET) sequence involving either one of the proton donors. However, water can be an effective CPET donor or acceptor (86–88), and we cannot rule out its participation explicitly, especially if H-bonding of water and CO₂ induces an early CPET transition state that may not give rise to an appreciable KIE. CPET sequences have been shown to give rise to appreciable H/D KIEs in surface electrochemical reactions (89–92), which we do not observe for CDR catalysis on Au (Fig. 3*D*). Instead, over the potential range probed in this study, we postulate that CO₂ activation on Au proceeds by an ET/PT mechanism with rate-limiting ET. Because the thermodynamic potential for outer-sphere reduction of CO₂ to its radial anion, CO₂^{•-}, is at −1.90 V in water (93), which is at least 1.10 V more negative than the top end of the linear Tafel range, we postulate that surface adsorption to Au imparts dramatic stabilization of the adsorbed ET intermediate and enables an ET/PT pathway. Whereas computational studies typically probe the energetics for adsorption of the neutral COOH intermediate (22, 27, 28), our findings suggest that the adsorption energy of COO⁻ is a better descriptor of the rate of CO₂ activation on Au.

The population of surface active sites for CDR (θ_{CDR}) on Au is fractional. An estimate of θ_{CDR} is provided by quantifying the population of CO_{bridge} species on the Au surface under catalytic conditions (Fig. 2). Because these CO species are bound irreversibly, we postulate that they act as inert spectators during CDR catalysis. Analyses of the stripping charge associated with CO oxidation, described above, reveal a surface coverage of CO_{bridge} of ~0.2. This high coverage suggests that CO_{bridge} species may decorate a combination of surface defects, basal planes, and/or reconstructed surface regions. The remaining surface fraction, ~0.8, not bound by CO_{bridge} places an upper limit on θ_{CDR} . Although these studies provide no direct insight into the active sites responsible for CDR catalysis, they are consistent with the emerging notion that CDR is mediated by minority surface features existent at Au step edges (22, 30, 31) or grain boundaries (56). Because we observe CO_{atop} adsorption in equilibrium with CO_g, we postulate that CO_g production proceeds through the intermediacy of CO_{atop} species, which rapidly desorb from the surface (Fig. 4*A*).

H₂ Production Is Dependent on the Proton Donor Environment. The relationship between potential and the rate of H₂ evolution (j_{H_2}) was probed over the same potential range as CDR, −0.80 to −1.00 V, corresponding to η between 0.80 and 1.00 V for HER. These data taken together with studies of reaction orders with respect to $[\text{HCO}_3^-]$, pH, and P_{CO} provide the basis for mechanistic interpretation of H₂ evolution occurring simultaneously with CDR

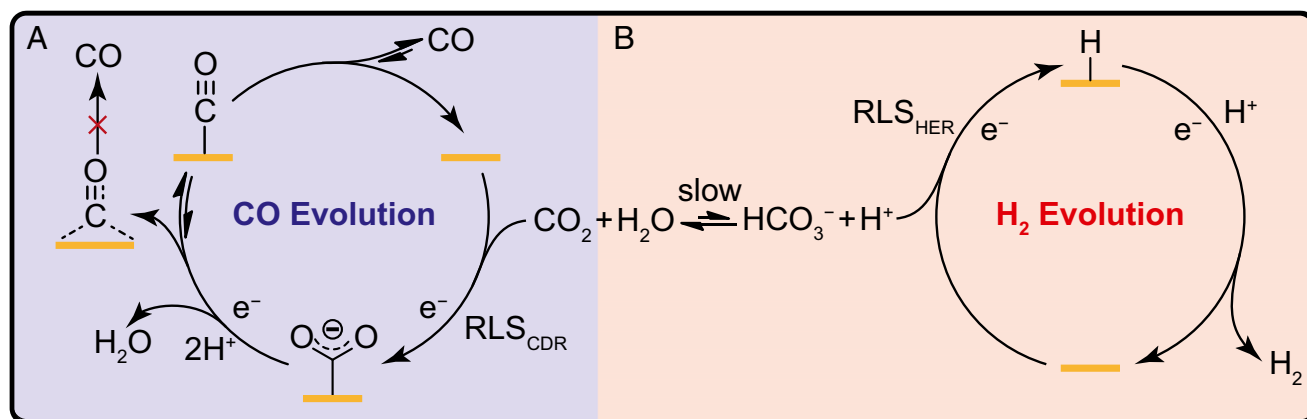


Fig. 4. Proposed mechanisms for (A) CO evolution (blue) and (B) concurrent H₂ evolution (red) on polycrystalline Au surfaces. Proposed rate-limiting steps (RLS) indicated for both reactions.

on polycrystalline Au surfaces. Fig. S7 shows that j_{H_2} is significantly affected by the rotation rate of the working electrode at applied potentials of -0.80 , -0.90 , and -1.00 V in CO_2 -saturated 0.1 M NaHCO_3 , showing that j_{H_2} is convoluted by mass transport limitations under these conditions. For the same reaction occurring in 1 M NaHCO_3 , however, the rotation rate dependence is greatly suppressed (Fig. S7). Thus, data taken in CO_2 -saturated 0.1 M NaHCO_3 are interpreted after accounting for mass transfer effects by extrapolating Koutecký–Levich (KL) plots (Fig. S7A) of $j_{\text{H}_2}^{-1}$ vs. $\omega^{-1/2}$ to the y-intercept, representing infinite rotation rate, to extract activation-controlled j_{H_2} values. Conversely, data recorded in CO_2 -saturated 1 M NaHCO_3 at $2,000$ rpm are taken as direct measurements of activation-controlled HER and overlaid with data analyzed using KL extrapolation (Fig. S8).

The Tafel behavior for HER is highly dependent on the proton donor environment. In Fig. 5A, we observe that the KL-extrapolated Tafel slope of 380 mV/dec for j_{H_2} in CO_2 -saturated 0.1 M NaHCO_3 is 170 mV/dec higher than the 210 -mV/dec slope observed in CO_2 -saturated 1 M NaHCO_3 . The high Tafel slope measured in CO_2 -saturated 0.1 M NaHCO_3 , where incremental excursions in η do not significantly increase the rate, implies that rate-limiting chemical steps gate HER rather than ET (81). The lower Tafel slope observed in CO_2 -saturated 1 M NaHCO_3 suggests a mechanism operative by rate-limiting single ET, with β equaling 0.3 (see above discussion for j_{CO}). Although Marcus theory would predict $\beta = 0.5$ for rate-limiting, outer-sphere, single-ET, transfer coefficients as low as 0.3 have been observed for inner-sphere electrochemical reactions involving rate-limiting ET (40, 94) and have also been predicted theoretically (95, 96). The observed changes in Tafel slope with bicarbonate concentration are further supported by the observation that j_{H_2} is invariant with η at low $[\text{HCO}_3^-]$ (0.03 mM), whereas j_{H_2} becomes highly dependent on η at higher concentrations (1 M) (Fig. 5B). We note that this experiment, however, is not a direct probe of the explicit bicarbonate order on j_{H_2} , because under CO_2 saturation conditions, varying the bicarbonate concentration

by 1 dec changes the bulk pH by 1 unit (18). Thus, extracting the explicit bicarbonate order requires the ability to hold two of three parameters in the CO_2 -bicarbonate-pH equilibrium constant, which cannot be achieved experimentally while maintaining this equilibrium. Given this convolution, we take the values of the bicarbonate order as approximate. We stress that this convolution was simplified when examining the dependence of j_{CO} on bicarbonate concentration (Fig. 3C), because j_{CO} is zeroth order in both bicarbonate and pH. Nevertheless, HER is forward order in bicarbonate at -0.80 and -0.90 V (Fig. 5B), suggesting that the anion is a viable proton donor for the reaction. In contrast, the explicit dependence of HER catalysis on pH can be obtained, assuming that CO_2 is not a direct reaction participant in HER. Under fixed $[\text{HCO}_3^-]$, we varied the pH by modulating the P_{CO_2} and found that j_{H_2} exhibits an inverse order dependence on the pH of the bulk electrolyte (Fig. 5C), suggesting that hydronium ions, as has been previously reported (97), or carbonic acid, which could be formed in minor equilibrium (98, 99), are also viable proton donors for this reaction. Together, the data suggest that hydronium, carbonic acid, and bicarbonate are viable proton donors and show that the rate of HER is highly dependent on the buffering strength.

The rate of HER is invariant with P_{CO} . In Fig. 5D, we observe that j_{H_2} is independent of P_{CO} , suggesting that equilibrium CO dissociation does not precede H adsorption. Given the precedent that a variety of Au surface facets can support HER catalysis in the absence of CO (100), we expect that surface sites that are not bound by CO under these conditions remain competent for HER, provided that the proton donor concentrations are sufficiently high. The order data imply that j_{H_2} , like CO production, is not gated by equilibrium dissociation of CO .

The data in Fig. 5 imply an electrochemical rate law described by the following equation (also shown schematically in Fig. 4B):

$$j_{\text{H}_2} = k_2 \theta_{\text{HER}} [\text{BH}]^x \exp \frac{\beta e F}{RT} + k_3 [\text{BH}]^x, \quad [2]$$

where k_2 and k_3 are potential-independent constants. The rate expression shows forward-order dependence in proton donor, but we refrain from assigning the proton donor as bicarbonate, carbonic acid, or hydronium, because they may all be competent donors depending on the buffer strength and overpotential. Thus, we denote these viable donors cumulatively as BH. Although we note that minority proton donors, such as carbonic acid and hydronium, are expected to be depleted in the diffusion layer during steady-state catalysis, we stress that they can be readily replenished by rapid PT from majority buffer constituents or autoionization of water. Additionally, although we observe reaction orders in BH, the value of the order scales between 0.05 and 0.55 for bicarbonate and between -0.19 and -0.70 for pH depending on the applied potential. Despite the high population of CO on the surface (see above), the rate expression for HER is zeroth order in CO . This rate law also includes an exponential term that captures the potential-dependent rate of an irreversible single ET step. At low bicarbonate concentration, we observe a higher Tafel slope, leading us to include a second term in the rate expression that carries no potential dependence and is, instead, gated by a rate-limiting chemical step that still carries BH dependence. In Eq. 2, θ_{HER} is defined as the surface coverage of HER active sites responsible for the first term in the rate expression.

The rate expression shown in Eq. 2 is consistent with a mechanistic model for HER catalysis occurring simultaneously with CDR that involves rate-limiting ET to hydronium, carbonic acid, or bicarbonate to form an adsorbed Au–H species at high bicarbonate concentrations. This Au–H intermediate undergoes rapid one ET, one PT or recombination with another Au–H to generate H_2 and regenerate the surface site for subsequent turnover (Fig. 4B). This mechanism is consistent with the fact that Au–H species have not been spectroscopically observed to date, suggesting a low population of this intermediate in contrast to HER on Pt, which

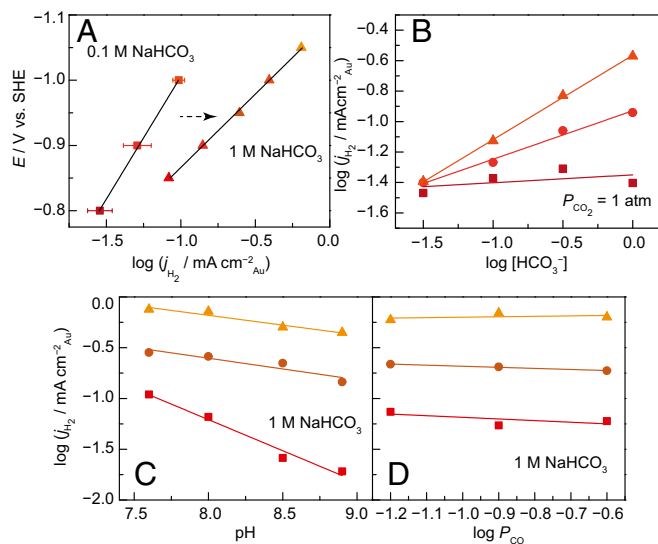


Fig. 5. Electrokinetic data for H_2 evolution catalysis. (A) KL-corrected Tafel plot for HER in CO_2 -saturated 0.1 M NaHCO_3 and raw Tafel plot for HER in CO_2 -saturated 1 M NaHCO_3 . The error bars correspond to the errors in the y-intercept obtained from least squares fitting of the data in Fig. S7A. (B) Bicarbonate concentration dependence of HER partial catalytic current density at -0.80 V (dark red), -0.90 V (orange), and -1.00 V (light orange). (C) pH and (D) P_{CO} dependence of HER on a Au RCE ($2,000$ rpm) at constant potentials of -0.85 V (red), -0.95 V (brown), and -1.05 V (dark yellow) in CO_2 -saturated 1 M NaHCO_3 electrolyte.

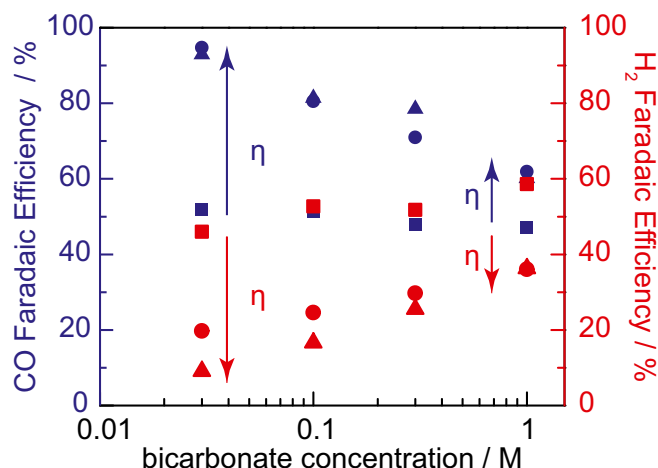


Fig. 6. CO (blue) vs. H₂ (red) Faradaic efficiency at -0.80 V (■), -0.90 V (●), and -1.00 V (▲) as a function of bicarbonate electrolyte concentration.

exhibits a high H coverage during catalysis (101). At lower bicarbonate concentrations, the second term dominates, limiting the rate of HER, which we postulate to be related to slow CO₂–bicarbonate equilibration steps (98, 99) that become competitive with the rate of PT to the surface at lower buffering strength and overpotentials. Nonetheless, the ensemble rate of HER is strongly dependent on the proton donor environment in a way that CDR catalysis is not.

Concluding Remarks

CDR catalysis at a metal electrode is an ensemble phenomenon that arises from the complex dynamics of surface adsorbates, intrinsic reaction kinetics, proton-coupled ET dynamics, and concentration gradients that develop at the interface. Herein, we have used a combination of electrochemical kinetics and in situ IR spectroscopy to parse these effects, and we have explicitly accounted for diffusional gradients by comparing experimental data collected on static and rotating electrodes. We find, for CDR and HER conducted on polycrystalline Au in CO₂-saturated bicarbonate electrolytes, that (i) the surfaces of Au electrodes consist of a high population of spectator CO_{bridge} species, (ii) CDR is gated by rate-limiting ET to CO₂ and is not dependent on the proton donor environment, (iii) HER is strongly dependent on the proton donor environment, (iv) the observed transfer coefficients for CDR are higher than those for HER, and (v) the intrinsic activation-controlled kinetics of CDR and HER are augmented by interfacial diffusional gradients that serve to suppress HER preferentially relative to CDR.

Together, these factors determine the critical parameters—proton donor concentration and applied overpotential (η)—that dictate catalyst selectivity. The effects of these two parameters on reaction selectivity are illustrated specifically in Fig. 6. Because of the intrinsically lower Tafel slope for CDR vs. HER, higher η favors CO (Fig. 6, blue) over H₂ evolution (Fig. 6, red) at a given bicarbonate concentration. In addition, accelerated rates of proton consumption with increased η serve to further decelerate the rate of HER as the proton donor concentration is decreased proximate to the surface. Because CDR is insensitive to the proton

donor environment, changes in the interfacial proton activity do not augment the rate of CO production. Furthermore, CO₂ equilibration with bicarbonate is hindered by slow CO₂ hydration kinetics [24-s half-life (99)], preserving a high interfacial CO₂ concentration, despite an elevated local pH. As a result, at modest η (Fig. 6, ■), similar rates of CDR and HER are observed irrespective of bicarbonate concentrations, whereas at higher η (Fig. 6, ● and ▲), lower bicarbonate concentrations serve to significantly suppress HER, enhancing selectivity. These mechanistic insights predict that CDR selectivity can be enhanced over a wider potential range by amplifying proton depletion effects within a porous electrode, a notion supported by our recent studies on ordered porous Au inverse opals (41). Interestingly, similar suppression of HER has been shown to enhance CDR selectivity in molecular catalytic systems (102).

Our results establish the value of combining electrokinetic experiments with in situ IR studies to gain a molecular-level understanding of complex reactions, such as CDR. Spectroscopic data reveal that spectator CO_{bridge} species occupy a high population of the Au surface, consistent with the notion that catalysis proceeds at a minority fraction of surface sites. Taken together with electrochemical kinetic data, this work establishes a comprehensive model of the interfacial structure and reactivity of Au under catalytically relevant conditions, which highlights the divergent proton coupling requirements of CDR and HER as key drivers of selectivity in fuel formation.

Materials and Methods

Au films for in situ SEIRAS analyses were synthesized using an electroless plating technique (49). Handling procedures for the Au film, foil, and RCE are reported in *SI Materials and Methods*, and their electrochemically active surface area and surface faceting are shown in Figs. S1 and S5, respectively.

SEIRAS measurements were conducted using an EG&G PAR Model 263A Potentiostat and a Bio-Rad FTS-60A/896 FTIR Spectrometer equipped with an HgCdTe (MCT) Detector and a homemade single-reflection accessory. The details of the ATR-SEIRAS cell configuration have been previously reported (45–48, 59, 103). CO₂ or CO₂/CO mixtures were continuously delivered to a three-compartment spectroelectrochemical cell containing purified (104) 100 mM NaHCO₃ during measurements. Spectra were sequentially acquired with a spectral resolution of 4 cm^{−1} at every 0.76-s interval for cyclic voltammetry measurements (Fig. 1) or 0.58-s interval (Fig. S3) for chronoamperometry measurements. A single-beam spectrum collected at the starting potential was used as the reference spectrum. Details of electrochemical methods used are further described in *SI Materials and Methods*.

Electrokinetic measurements were conducted using a Gamry REF 600 Potentiostat and an in-line gas chromatograph (Multi-Gas Analyzer #3; SRI Instruments) equipped with a thermal conductivity detector, methanizer, and flame ionization detector in series after Molsieve 13x and Haysep D Columns. CO₂, CO₂/Ar, or CO₂/Ar/CO mixtures were continuously delivered to an airtight H cell containing purified (104) NaHCO₃ or NaDCO₃ (preparation is described in *SI Materials and Methods*) during measurements. GC traces were collected every 20 min, and the evolved CO or H₂ gases were converted to partial current densities as described in *SI Materials and Methods*.

ACKNOWLEDGMENTS. We thank Anthony Shoji Hall for helpful discussions and Tomohiro Fukushima for facilitating spectroscopic studies conducted at Hokkaido University (HU). A.W. and Y.S. thank the Massachusetts Institute of Technology (MIT) International Science and Technology Initiatives and the Hayashi Seed Grant for Travel Funds to HU. This research was supported by Air Force Office of Scientific Research under AFOSR Award FA9550-15-1-0135 and by the MIT Department of Chemistry through junior faculty funds (Y.S.). Work at HU was partially supported by the New Energy and Industrial Technology Development Organization. A.W. is supported by a Graduate Research Fellowship from the National Science Foundation.

- Hartwig JF, Walsh PJ (2010) Principles of catalysis. *Organotransition Metal Chemistry: From Bonding to Catalysis* (University Science Books, Mill Valley, CA), pp 539–574.
- Ferscht A (1998) *Structure and Mechanism in Protein Science: A Guide to Enzyme Catalysis and Protein Folding* (Freeman, New York).
- Lippard SJ, Berg JM (1994) *Principles of Bioinorganic Chemistry* (University Science Books, Mill Valley, CA).
- Lee SJ, McCormick MS, Lippard SJ, Cho U-S (2013) Control of substrate access to the active site in methane monooxygenase. *Nature* 494(7437):380–384.

- Fontecilla-Camps JC, Volbeda A, Cavazza C, Nicolet Y (2007) Structure/function relationships of [NiFe]- and [FeFe]-hydrogenases. *Chem Rev* 107(10):4273–4303.
- Somorjai GA, Contreras AM, Montano M, Rioux RM (2006) Clusters, surfaces, and catalysis. *Proc Natl Acad Sci USA* 103(28):10577–10583.
- Somorjai GA, Park JY (2008) Molecular factors of catalytic selectivity. *Angew Chem Int Ed Engl* 47(48):9212–9228.
- Zaera F (2010) The new materials science of catalysis: Toward controlling selectivity by designing the structure of the active site. *J Phys Chem Lett* 1(3): 621–627.

9. Thomas JM, Thomas WJ (1967) *Introduction to the Principles of Heterogeneous Catalysis* (Academic, London).
10. Zaera F (2002) Outstanding mechanistic questions in heterogeneous catalysis. *J Phys Chem B* 106(16):4043–4052.
11. Gao X, Hamelin A, Weaver MJ (1991) Potential-dependent reconstruction at ordered Au(100)-aqueous interfaces as probed by atomic-resolution scanning tunneling microscopy. *Phys Rev Lett* 67(5):618–621.
12. Wasileski SA, Koper MTM, Weaver MJ (2002) Field-dependent electrode-adsorbate bonding: Sensitivity of vibrational Stark effect and binding energetics to nature of surface coordination. *J Am Chem Soc* 124(11):2796–2805.
13. Gileadi E (1993) *Electrode Kinetics for Chemists, Chemical Engineers, and Materials Scientists* (Wiley-VCH, New York).
14. Olah GA, Prakash GKS, Goepfert A (2011) Anthropogenic chemical carbon cycle for a sustainable future. *J Am Chem Soc* 133(33):12881–12898.
15. Whipple DT, Kenis PJA (2010) Prospects of CO₂ utilization via direct heterogeneous electrochemical reduction. *J Phys Chem Lett* 1(24):3451–3458.
16. Appel AM, et al. (2013) Frontiers, opportunities, and challenges in biochemical and chemical catalysis of CO₂ fixation. *Chem Rev* 113(8):6621–6658.
17. Kondratenko EV, Mul G, Baltrusaitis J, Larrazábal GO, Pérez-Ramírez J (2013) Status and perspectives of CO₂ conversion into fuels and chemicals by catalytic, photocatalytic and electrocatalytic processes. *Energy Environ Sci* 6(11):3112–3135.
18. Hori Y (2008) Electrochemical CO₂ reduction on metal electrodes. *Modern Aspects of Electrochemistry*, eds Vayenas C, White R, Gamboa-Aldeco M (Springer, New York), pp 89–189.
19. Benson EE, Kubiak CP, Sathrum AJ, Smieja JM (2009) Electrocatalytic and homogeneous approaches to conversion of CO₂ to liquid fuels. *Chem Soc Rev* 38(1):89–99.
20. Rosenthal J (2014) Progress toward the electrocatalytic production of liquid fuels from carbon dioxide. *Progress in Inorganic Chemistry*, ed Karlin KD (John Wiley & Sons, Hoboken, NJ), pp 299–338.
21. Sabatier P (1911) Hydrogénations et déshydrogénations par catalyse. *Berichte der Deutschen Chemischen Gesellschaft* 44(3):1984–2001.
22. Zhu W, et al. (2013) Monodisperse Au nanoparticles for selective electrocatalytic reduction of CO₂ to CO. *J Am Chem Soc* 135(45):16833–16836.
23. Peterson AA (2015) Optimizing electrocatalyst selectivity for CO₂ reduction over H₂ evolution. *ECS Trans* 66(3):41–52.
24. Zhang Y-J, Sethuraman V, Michalsky R, Peterson AA (2014) Competition between CO₂ reduction and H₂ evolution on transition-metal electrocatalysts. *ACS Catal* 4(10):3742–3748.
25. Zhang Y-J, Peterson AA (2015) Oxygen-induced changes to selectivity-determining steps in electrocatalytic CO₂ reduction. *Phys Chem Chem Phys* 17(6):4505–4515.
26. Calle-Vallejo F, Koper MTM (2013) Theoretical considerations on the electroreduction of CO to C₂ species on Cu(100) electrodes. *Angew Chem Int Ed Engl* 52(28):7282–7285.
27. Hansen HA, Varley JB, Peterson AA, Nørskov JK (2013) Understanding trends in the electrocatalytic activity of metals and enzymes for CO₂ reduction to CO. *J Phys Chem Lett* 4(3):388–392.
28. Peterson AA, Nørskov JK (2012) Activity descriptors for CO₂ electroreduction to methane on transition-metal catalysts. *J Phys Chem Lett* 3(2):251–258.
29. Shi C, Hansen HA, Lausche AC, Nørskov JK (2014) Trends in electrochemical CO₂ reduction activity for open and close-packed metal surfaces. *Phys Chem Chem Phys* 16(10):4720–4727.
30. Mistry H, et al. (2014) Exceptional size-dependent activity enhancement in the electroreduction of CO₂ over Au nanoparticles. *J Am Chem Soc* 136(47):16473–16476.
31. Zhu W, et al. (2014) Active and selective conversion of CO₂ to CO on ultrathin Au nanowires. *J Am Chem Soc* 136(46):16132–16135.
32. Lu Q, Rosen J, Jiao F (2015) Nanostructured metallic electrocatalysts for carbon dioxide reduction. *ChemCatChem* 7(1):38–47.
33. Koverga AA, Frank S, Koper MTM (2013) Density functional theory study of electric field effects on CO and OH adsorption and co-adsorption on gold surfaces. *Electrochim Acta* 101:244–253.
34. Rodríguez P, Koverga AA, Koper MTM (2010) Carbon monoxide as a promoter for its own oxidation on a gold electrode. *Angew Chem Int Ed Engl* 49(7):1241–1243.
35. Gupta N, Gattrell M, MacDougall B (2005) Calculation for the cathode surface concentrations in the electrochemical reduction of CO₂ in KHCO₃ solutions. *J Appl Electrochem* 36(2):161–172.
36. Delacourt C, Ridgway PL, Newman J (2010) Mathematical modeling of CO₂ reduction to CO in aqueous electrolytes. *J Electrochem Soc* 157(12):B1902–B1910.
37. Kas R, Kortlever R, Yilmaz H, Koper MTM, Mul G (2015) Manipulating the hydrocarbon selectivity of copper nanoparticles in CO₂ electroreduction by process conditions. *ChemElectroChem* 2(3):354–358.
38. Varela AS, Kroschel M, Reier T, Strasser P (2016) Controlling the selectivity of CO₂ electroreduction on copper: The effect of the electrolyte concentration and the importance of the local pH. *Catal Today* 260:8–13.
39. Kortlever R, Shen J, Schouten KJP, Calle-Vallejo F, Koper MTM (2015) Catalysts and reaction pathways for the electrochemical reduction of carbon dioxide. *J Phys Chem Lett* 6(20):4073–4082.
40. Hori Y, Takahashi R, Yoshinami Y, Murata A (1997) Electrochemical reduction of CO at a copper electrode. *J Phys Chem B* 101(36):7075–7081.
41. Hall AS, Yoon Y, Wuttig A, Surendranath Y (2015) Mesostructure-induced selectivity in CO₂ reduction catalysis. *J Am Chem Soc* 137(47):14834–14837.
42. Noda H, Ikeda S, Yamamoto A, Einaga H, Ito K (1995) Kinetics of electrochemical reduction of carbon dioxide on a gold electrode in phosphate buffer solutions. *Bull Chem Soc Jpn* 68(7):1889–1895.
43. Hori Y, Murata A, Kikuchi K, Suzuki S (1987) Electrochemical reduction of carbon dioxides to carbon monoxide at a gold electrode in aqueous potassium hydrogen carbonate. *J Chem Soc Chem Commun* 10(10):728–729.
44. Osawa M, Ikeda M (1991) Surface-enhanced infrared absorption of p-nitrobenzoic acid deposited on silver island films: Contributions of electromagnetic and chemical mechanisms. *J Phys Chem* 95(24):9914–9919.
45. Osawa M (1997) Dynamic processes in electrochemical reactions studied by surface-enhanced infrared absorption spectroscopy (SEIRAS). *Bull Chem Soc Jpn* 70(12):2861–2880.
46. Osawa M (2002) Surface enhanced infrared absorption spectroscopy. *Handbook of Vibrational Spectroscopy*, eds Chalmers JM, Griffiths PR (Wiley-VCH, Chichester, United Kingdom), pp 785–800.
47. Osawa M (2006) In-situ surface-enhanced infrared spectroscopy of the electrode/solution interface. *Diffraction and Spectroscopic Methods in Electrochemistry, Advances in Electrochemical Science and Engineering*, eds Alkire RC, Kolb DM, Lipkowski J, Ross PN (Wiley-VCH, New York), Vol 9, pp 269–314.
48. Osawa M (2001) Surface-enhanced infrared absorption. *Near-Field Optics and Surface Plasmon Polaritons. Topics in Applied Physics*, ed Kawata S (Springer, Berlin), Vol 81, pp 163–187.
49. Miyake H, Ye S, Osawa M (2002) Electroless deposition of gold thin films on silicon for surface-enhanced infrared spectroelectrochemistry. *Electrochem Commun* 4(12):973–977.
50. Chang RK, Furtak TE, eds (1982) *Surface Enhanced Raman Scattering* (Plenum, New York).
51. Moskovits M (1985) Surface-enhanced spectroscopy. *Rev Mod Phys* 57(3):783–826.
52. Miki A, Ye S, Osawa M (2002) Surface-enhanced IR absorption on platinum nanoparticles: An application to real-time monitoring of electrocatalytic reactions. *Chem Commun (Camb)* (14):1500–1501.
53. Leung LWH, Wiekowski A, Weaver MJ (1988) In situ infrared spectroscopy of well-defined single-crystal electrodes: Adsorption and electrooxidation of carbon monoxide on platinum(111). *J Phys Chem* 92(24):6985–6990.
54. Samjeské G, Komatsu K, Osawa M (2009) Dynamics of CO oxidation on a polycrystalline platinum electrode: A time-resolved infrared study. *J Phys Chem C* 113(23):10222–10228.
55. Weaver MJ, et al. (1992) Evaluation of absolute saturation coverages of carbon monoxide on ordered low-index platinum and rhodium electrodes. *J Electroanal Chem (Lausanne)* 327(1–2):247–260.
56. Chen Y, Li CW, Kanan MW (2012) Aqueous CO₂ reduction at very low overpotential on oxide-derived Au nanoparticles. *J Am Chem Soc* 134(49):19969–19972.
57. Arihara K, Kitamura F, Ohsaka T, Tokuda K (2001) Characterization of the adsorption state of carbonate ions at the Au(111) electrode surface using in situ IRAS. *J Electroanal Chem (Lausanne)* 510(1–2):128–135.
58. Berná A, et al. (2004) Structural and Spectroelectrochemical Study of Carbonate and Bicarbonate Adsorbed on Pt(111) and Pd/Pt(111) Electrodes. *J Phys Chem B* 108(46):17928–17939.
59. Ataka K, Yotsuyanagi T, Osawa M (1996) Potential-dependent reorientation of water molecules at an electrode/electrolyte interface studied by surface-enhanced infrared absorption spectroscopy. *J Phys Chem* 100(25):10664–10672.
60. Ataka K, Osawa M (1998) In situ infrared study of water–sulfate coadsorption on gold(111) in sulfuric acid solutions. *Langmuir* 14(4):951–959.
61. Osawa M, Tsumura M, Mogami H, Samjeské G, Yamakata A (2008) Structure of water at the electrified platinum–water interface: A study by surface-enhanced infrared absorption spectroscopy. *J Phys Chem C* 112(11):4248–4256.
62. Lambert DK (1996) Vibrational Stark effect of adsorbates at electrochemical interfaces. *Electrochim Acta* 41(5):623–630.
63. Jinnouchi R, Hatanaka T, Morimoto Y, Osawa M (2013) Stark effect on vibration frequencies of sulfate on Pt(111) electrode. *Electrochim Acta* 101:254–261.
64. Lambert DK (1984) Stark effect of adsorbate vibrations. *Solid State Commun* 51(5):297–300.
65. Beden B, Bewick A, Kunimatsu K, Lamy C (1982) Infrared study of adsorbed species on electrodes: Adsorption of carbon monoxide on Pt, Rh and Au. *J Electroanal Chem Interfacial Electrochem* 142(1–2):345–356.
66. Sun S-G, Cai W-B, Wan L-J, Osawa M (1999) Infrared absorption enhancement for CO adsorbed on Au films in perchloric acid solutions and effects of surface structure studied by cyclic voltammetry, scanning tunneling microscopy, and surface-enhanced IR spectroscopy. *J Phys Chem B* 103(13):2460–2466.
67. Chang SC, Hamelin A, Weaver MJ (1991) Dependence of the electrooxidation rates of carbon monoxide at gold on the surface crystallographic orientation: A combined kinetic-surface infrared spectroscopic study. *J Phys Chem* 95(14):5560–5567.
68. Blizanac BB, Arenz M, Ross PN, Marković NM (2004) Surface electrochemistry of CO on reconstructed gold single crystal surfaces studied by infrared reflection absorption spectroscopy and rotating disk electrode. *J Am Chem Soc* 126(32):10130–10141.
69. Hussain A, Curulla Ferré D, Gracia J, Nieuwenhuys BE, Niemantsverdriet JW (2009) DFT study of CO and NO adsorption on low index and stepped surfaces of gold. *Surf Sci* 603(17):2734–2741.
70. Shubina TE, Hartnig C, Koper MTM (2004) Density functional theory study of the oxidation of CO by OH on Au(110) and Pt(111) surfaces. *Phys Chem Chem Phys* 6(16):4215–4221.
71. Yim W-L, et al. (2007) Universal phenomena of CO adsorption on gold surfaces with low-coordinated sites. *J Phys Chem C* 111(1):445–451.
72. Mehmood F, Kara A, Rahman TS, Henry CR (2009) Comparative study of CO adsorption on flat, stepped, and kinked Au surfaces using density functional theory. *Phys Rev B* 79(7):075422.
73. Rodríguez P, García-Araez N, Koverga A, Frank S, Koper MTM (2010) CO electrooxidation on gold in alkaline media: A combined electrochemical, spectroscopic, and DFT study. *Langmuir* 26(14):12425–12432.
74. Hartwig JF (2010) Carbon monoxide and related ligands. *Organotransition Metal Chemistry: From Bonding to Catalysis* (University Science Books, Mill Valley, CA), pp 27–33.

75. Bliznac BB, et al. (2004) Anion adsorption, CO oxidation, and oxygen reduction reaction on a Au(100) surface: The pH effect. *J Phys Chem B* 108(2):625–634.
76. Chang S-C, Hamelin A, Weaver MJ (1990) Reactive and inhibiting adsorbates for the catalytic electrooxidation of carbon monoxide on gold (210) as characterized by surface infrared spectroscopy. *Surf Sci* 239(3):L543–L547.
77. Kita H, Nakajima H, Hayashi K (1985) Electrochemical oxidation of CO on Au in alkaline solution. *J Electroanal Chem Interfacial Electrochem* 190(1–2):141–156.
78. Nakajima H, Kita H, Kunitatsu K, Aramata A (1986) Infrared spectra of carbon monoxide adsorbed on a smooth gold electrode Part I. EMIRS spectra in acid and alkaline solutions. *J Electroanal Chem Interfacial Electrochem* 201(1):175–186.
79. Kirova-Eisner E, Gileadi E (1976) The rotating cone electrode. *J Electrochem Soc* 123(1):22–24.
80. Rouya E, Cattarin S, Reed ML, Kelly RG, Zangari G (2012) Electrochemical characterization of the surface area of nanoporous gold films. *J Electrochem Soc* 159(4):K97–K102.
81. Gileadi E (2011) *Physical Electrochemistry, Fundamentals, Techniques and Applications* (Wiley-VCH, Weinheim, Germany).
82. Bard AJ, Faulkner LR (2001) *Spectroelectrochemistry and other coupled characterization methods. Electrochemical Methods* (Wiley, New York), 2nd Ed, p 700.
83. Hori Y, Wakebe H, Tsukamoto T, Koga O (1994) Electrocatalytic process of CO selectivity in electrochemical reduction of CO₂ at metal electrodes in aqueous media. *Electrochim Acta* 39(11–12):1833–1839.
84. Ikeda S, Takagi T, Ito K (1987) Selective formation of formic acid, oxalic acid, and carbon monoxide by electrochemical reduction of carbon dioxide. *Bull Chem Soc Jpn* 60(7):2517–2522.
85. Vassiliev YB, Bagotsky VS, Osetrova NV, Khazova OA, Mayorova NA (1985) Electroreduction of carbon dioxide. *J Electroanal Chem Interfacial Electrochem* 189(2):271–294.
86. Costentin C, Robert M, Savéant J-M (2007) Concerted proton-electron transfer reactions in water. are the driving force and rate constant depending on pH when water acts as proton donor or acceptor? *J Am Chem Soc* 129(18):5870–5879.
87. Bonin J, Costentin C, Louault C, Robert M, Savéant J-M (2011) Water (in water) as an intrinsically efficient proton acceptor in concerted proton electron transfers. *J Am Chem Soc* 133(17):6668–6674.
88. Costentin C (2008) Electrochemical approach to the mechanistic study of proton-coupled electron transfer. *Chem Rev* 108(7):2145–2179.
89. Chen G, Delafuente DA, Sarangapani S, Mallouk TE (2001) Combinatorial discovery of bifunctional oxygen reduction — water oxidation electrocatalysts for regenerative fuel cells. *Catal Today* 67(4):341–355.
90. Conway BE (1960) Kinetics of electrolytic hydrogen and deuterium evolution. *Proc R Soc Lond A Math Phys Eng Sci* 256(1284):128–144.
91. Kuhn AT, Byrne M (1971) The hydrogen- and deuterium-evolution reactions on gold in acid solutions. *Electrochim Acta* 16(3):391–399.
92. Gagliardi CJ, Jurs JW, Thorp HH, Meyer TJ (2011) Surface activation of electrocatalysis at oxide electrodes. Concerted electron-proton transfer. *Inorg Chem* 50(6):2076–2078.
93. Schwarz HA, Dodson RW (1989) Reduction potentials of CO₂^{•−} and the alcohol radicals. *J Phys Chem* 93(1):409–414.
94. Soderberg JN, Co AC, Sirk AHC, Birss VI (2006) Impact of porous electrode properties on the electrochemical transfer coefficient. *J Phys Chem B* 110(21):10401–10410.
95. Venkataraman C, Soudackov AV, Hammes-schiffer S (2008) Theoretical formulation of nonadiabatic electrochemical proton-coupled electron transfer at metal - solution interfaces. *J Phys Chem C Nanomater Interfaces* 112(32):12386–12397.
96. Hammes-Schiffer S (2009) Theory of proton-coupled electron transfer in energy conversion processes. *Acc Chem Res* 42(12):1881–1889.
97. Costentin C, Canales JC, Haddou B, Savéant J-M (2013) Electrochemistry of acids on platinum. Application to the reduction of carbon dioxide in the presence of pyridinium ion in water. *J Am Chem Soc* 135(47):17671–17674.
98. Adamczyk K, Prémont-Schwarz M, Pines D, Pines E, Nibbering ETJ (2009) Real-time observation of carbonic acid formation in aqueous solution. *Science* 326(5960):1690–1694.
99. Pocker Y, Bjorkquist DW (1977) Stopped-flow studies of carbon dioxide hydration and bicarbonate dehydration in water and water-d₂. Acid-base and metal ion catalysis. *J Am Chem Soc* 99(20):6537–6543.
100. Perez J, Gonzalez ER, Villullas HM (1998) Hydrogen evolution reaction on gold single-crystal electrodes in acid solutions. *J Phys Chem B* 102(52):10931–10935.
101. Kunitatsu K, Senzaki T, Samjeské G, Tsushima M, Osawa M (2007) Hydrogen adsorption and hydrogen evolution reaction on a polycrystalline Pt electrode studied by surface-enhanced infrared absorption spectroscopy. *Electrochim Acta* 52(18):5715–5724.
102. Elgrishi N, Chambers MB, Fontecave M (2015) Turning it off! Disfavoring hydrogen evolution to enhance selectivity for CO production during homogeneous CO₂ reduction by cobalt-terpyridine complexes. *Chem Sci* 6(4):2522–2531.
103. Osawa M, Ataka K, Yoshii K, Yotsuyanagi T (1993) Surface-enhanced infrared ATR spectroscopy for in situ studies of electrode/electrolyte interfaces. *J Electron Spectrosc Relat Phenom* 64–65:371–379.
104. Wuttig A, Surendranath Y (2015) Impurity ion complexation enhances carbon dioxide reduction catalysis. *ACS Catal* 5(7):4479–4484.
105. Hamelin A (1984) Underpotential deposition of lead on single crystal faces of gold. *J Electroanal Chem Interfacial Electrochem* 165(1–2):167–180.
106. Hamelin A, Lipkowski J (1984) Underpotential deposition of lead on gold single crystal faces. *J Electroanal Chem Interfacial Electrochem* 171(1–2):317–330.
107. Adzic R, Yeager E, Cahan BD (1974) Optical and electrochemical studies of underpotential deposition of lead on gold evaporated and single-crystal electrodes. *J Electrochem Soc* 121(4):474–484.
108. Wang Y, Laborda E, Ward KR, Tschulik K, Compton RG (2013) A kinetic study of oxygen reduction reaction and characterization on electrodeposited gold nanoparticles of diameter between 17 nm and 40 nm in 0.5 M sulfuric acid. *Nanoscale* 5(20):9699–9708.